Graphical Abstract

Performance of a tubular direct absorption solar collector with a carbon-based nanofluid

P.G. Struchalin,V. S. Yunin,K. V. Kutsenko,O. V. Nikolaev,A. A. Vologzhannikova,M. P. Shevelyova,O. S. Gorbacheva,B. V. Balakin

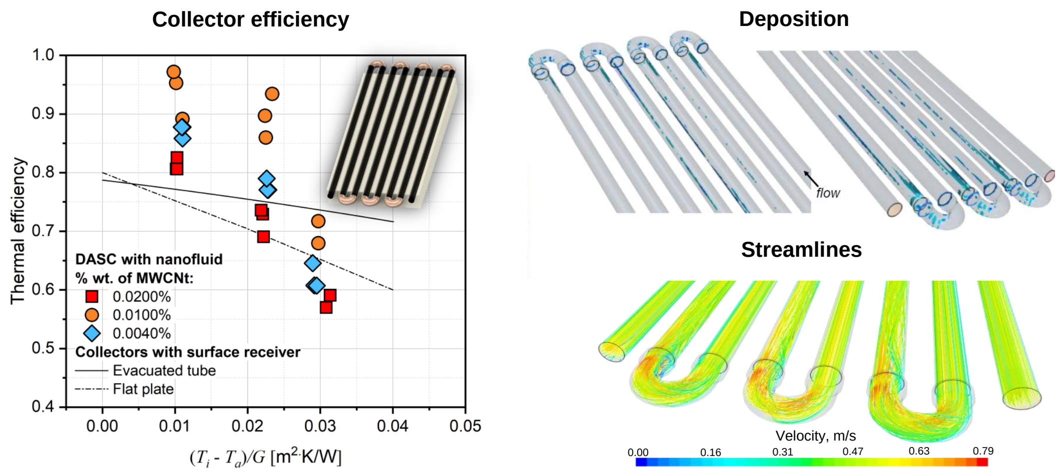

Highlights

Performance of a tubular direct absorption solar collector with a carbon-based nanofluid

P.G. Struchalin,V. S. Yunin,K. V. Kutsenko,O. V. Nikolaev,A. A. Vologzhannikova,M. P. Shevelyova,O. S. Gorbacheva,B. V. Balakin

- we test the performance of a nanofluid-based tubular DASC
- we alter the flow rate, the concentrations of nanoparticles, and the irradiation
- DASC demonstrates up to 38% better performance than an opaque collector
- we elucidate internals of DASC using the CFD
- we report details of nanofluid lifecycle in DASC

Performance of a tubular direct absorption solar collector with a carbon-based nanofluid

P.G. Struchalin[a,b,*], V. S. Yunin[a], K. V. Kutsenko[a], O. V. Nikolaev[c], A. A. Vologzhannikova[d], M. P. Shevelyova[d], O. S. Gorbacheva[e] and B. V. Balakin[b,a]

[a]*Department of Thermal Physics, National Research Nuclear University "Moscow Engineering Physics Institute", Kashirskoe highway 31, 115409 Moscow, Russia*

[b]*Department of Mechanical and Marine Engineering, Western Norway University of Applied Sciences, Postbox 7030, 5020 Bergen, Norway*

[c]*Skolkovo Institute of Science and Technology, Bolshoy Boulevard 30, bld. 1, 121205 Moscow, Russia*

[d]*Institute for Biological Instrumentation, Pushchino Scientific Center for Biological Research of the Russian Academy of Sciences, Pushchino, Moscow region, 142290, Russia*

[e]*LLC RL Test-Pushchino, Pushchino, Moscow region, 142290, Russia*

ARTICLE INFO

Keywords:
Direct absorption solar collector
Carbon nanotubes
Nanofluid
CFD
Solar collector

Abstract

Direct absorption solar collectors (DASC) with nanofluid represent a new direction in solar thermal technology that is simpler yet more efficient than conventional equipment. In this work, we report details of performance for a custom tubular DASC with a carbon-based nanofluid. The collector was tested experimentally following a standard procedure and using a multiphase CFD-model of the device. The experiments were carried out in a range of flow rates 2...10 l/min, nanoparticle concentrations 0.0015...0.082%wt., temperature differences (up to 29.3 degrees), and radiant heat fluxes. We found that, at a particle concentration of 0.01%, the collector demonstrated the average thermal efficiency of 80%. For the comparable temperature differences, the efficiency of DASC was 5.8...37.9% higher than a collector with similar geometry but a surface absorption of light energy.

The CFD-model, validated against our experiments, depicts flow patterns in the DASC focusing on nanoparticles' deposition. Less than 5% of particles deposit under local flow restrictions at flows above 6 l/min. The deposition patterns from the CFD-model correlate to the experimental observations.

1. Introduction

Solar energy has been showing sustainable development over the past decades. According to the data presented in the annual status report of the Bureau REN21 [1], at the end of 2019, the total capacity of solar power plants was 1 112.2 GW. Of this amount, 627 GW (56.4%) was electric power generated by solar photovoltaic plants, 6.2 GW (0.5%) was thermal power generated by solar concentrating systems, and 479 GW (43.1%) was thermal power from the solar collectors. The latter technology provides the most efficient solar energy collection and is considered an important source of renewable energy. According to the International Energy Agency, the world's annual growth of solar thermal supply is 10.9% [2]. This is the 4^{th} emerging renewable market after photovoltaics (PV), wind, and biogas.

Due to its high thermal efficiency, solar thermal generation works not only in the tropics but much further to the north in countries that are stereotypically distinguished by a lower solar energy potential. In fact, the technology is common in Scandinavia with over 1 GW_{th} solar collector capacities installed [3] and also in Canada which accommodates around 400 MW_{th} of solar thermal facilities [3].

The use of solar collectors in northern conditions raises problems concerning their efficiency and capital costs. In cold climates, solar collectors experience increased thermal leaks into the environment and an associated decrease of thermal efficiency. For the sustainable development of solar thermal energy in cold environments, it is necessary to improve the existing standard technology.

The main operating principle of conventional collectors is the convective transfer of heat from the receiver surface by the circulating fluid. The receiver, heated by solar radiation, is tailored in terms of thermal absorption and insulation. The disadvantage of such a system is the overheating of the receiver surface relative to the circulated coolant, which enhances thermal leaks into the environment. Many methods have been considered for optimising the design of solar collectors, aimed at reducing heat losses and increasing the heat transfer coefficient of the working fluid [4–11]. A novel and promising way to boost the efficiency of the collectors is to utilise nanofluids. The nanofluids in solar collectors increase the heat transfer coefficients compared to traditionally used water or water-glycol solutions. An alternative way to increase the performance of solar-to-thermal energy conversion systems is the joint use of direct absorption collectors

*Corresponding author
pstr@hvl.no (P.G. Struchalin)
ORCID(s):

Nomenclature

A	area [m^2]	C	coefficients
C_p	specific heat [J/kgK]	d	particle size [m]
D_p	pipe diameter [m]	D_B	diffusion coefficient [m^2/s]
e	enthalpy [J/kg]	F, M	force [N/m^3]
g	acceleration due to gravity [m/s^2]	G	radiant heat [W/m^2]
k	thermal conductivity [W/mK]	Kn	Knudsen number
k_b	Boltzmann constant [J/K]	l	lightpath [m]
m	mass [kg]	$\dot{m}$	mass flow [kg/s]
n	number density [1/m^3]	p	pressure [Pa]
q	internal heat generation [W/m^3]	r	reflectance
s	length of the pipes [m]	t	time [s]
T	temperature [K]	$\mathbf{T}$	shear stress [Pa/m]
v	velocity [m/s]	x	mass fraction
Greek symbols			
α	volume fraction	δ	Kronecker‘s function
κ	extinction coefficient [1/m]	μ	viscosity [Pa·s]
ρ	density [kg/m^3]	σ	Prandtl number
θ	reduced temperature	η	thermal efficiency
Subscripts, superscripts			
a	ambient	D	drag
eff	effective	f	final
i	inlet	in	initial
l	liquid	L	lift
nf	nanofluid	p	particle
th	thermophoresis	t	turbulent
vm	virtual mass		

with a nanofluid [12, 13]. Direct absorption solar collector (DASC) is a collector with a transparent receiver that allows for solar thermal energy to be absorbed directly by the working fluid.

Multiple studies have been carried out to examine the properties of solar radiation absorption by nanofluids of different compositions. These studies aimed to determine the absorption coefficients of visible, IR, and UV radiation in nanofluids, determining the integral indicators of thermal radiation absorption, the dynamics of nanofluid samples heating, and the temperature distribution in them during photothermal heating [14–20]. In these works, nanofluids demonstrate an advantage over the dispersing media, i.e., the base fluid. However, there are very few works that consider the practical implementation of nanofluids in DASC.

The volumetric absorption of solar energy in a water-glycol solution of Indian ink containing fine carbon particles was experimentally investigated in [21]. In this work, a spiral tubular DASC demonstrated thermal efficiency up to 77% when the concentration of ink was 3 g/l. The efficiency of the "black water"-based solar collector was compared with the efficiency of the water-based flat-plate solar collector, which was not, however, optimised for commercial use. The "black water" collector had up to 30% higher thermal efficiency than the flat-plate collector. The study by Minardi and Chuang is missing important aspects of the collector performance. Namely, the sensitivity of the process regarding the flow through the collector was not considered, nor did the authors investigate the deposition of the ink particles, which were obviously sized by several micrometers.

The paper [22] presents the experimental and numerical study of the DASC thermal efficiency. Nanofluids based on Texatherm oil with particles of TiO_2, Al_2O_3, Ag, Cu, SiO_2, C are considered in this work. Nanofluids were pumped through a lab-scale cylindrical DASC (10 cm x 2,5 cm), irradiated by the light of halogen lamps with a maximum intensity of up to 8000 W/m^2. The flow rates varied from 9.5 ml/min to 47.5 ml/min. It was found that nanofluids based on carbon, silver, and aluminum oxide particles increase the thermal efficiency of DASC the most. Hence, by using nanofluids with 0.01% vol. carbon particles or 0.5% aluminum oxide particles, the efficiency increases by 22.7

and 17.5%, respectively, relative to the efficiency of the same collector without nanoparticles but with the black coating of the inner surface of the glass. The authors stated that the efficiency strongly depended on the light flux and the flow rate. The concentration of particles affects the temperature distribution inside the collector, so it is necessary to avoid an intense overheating of nanofluid surface layers at high concentrations of particles. The influence of particle concentration on the DASC thermal efficiency was not considered.

The study by Gupta et al. [23] considers a flat direct absorption collector with an aqueous nanofluid based on particles of aluminum oxide Al_2O_3. As a result of their experiments, the maximum increase in the thermal efficiency of DASC when using a nanofluid with a particle concentration of 0.005% was 39.6% compared to the case of using pure water.

The article by Karami et al. [24] considers a flat DASC. A nanofluid with copper oxide particles based on a water-glycol solution (70% water + 30% ethylene glycol) was stabilised by polyvinylpyrrolidone. The ratio of the surfactant mass to the particle mass was 1:4. The nanofluid was dispersed for 60 minutes with an ultrasonic probe. It was found that nanofluid increases the DASC efficiency by 17% at a flow rate of 90 l/h and 100 ppm concentration of nanoparticles. The authors also compared nanofluid-operated DASC, the DASC with a blackened back surface and the base fluid as a working fluid. It has been found that the use of nanofluid-based DASC had 7...7.8% higher thermal efficiency. The next paper from this group [25] reports experiments with the same DASC. Water-glycol nanofluids (70:30) with carbon nanotubes at concentrations from 0 to 100 ppm were used. The experiments were carried out by irradiating the collector with solar radiation. The nanofluid flow rates varied from 0.9 to 1.5 l/min. As follows from the experiments, the collector with nanofluid demonstrates thermal efficiency up to 89.3%, which was higher than 45% obtained for the base case with a blackened back surface. In this work, the authors did not find the values of the flow rate and particle concentration (or their combination), resulting in the highest efficiency of the collector. Instead, it was only indicated how changes in the flow rate and the concentration affect the collector efficiency.

A flat DASC using nanofluid based on graphene nanohorns and deionised water was investigated in the work [26]. The nanofluid was prepared by dispersing nanohorns in water using ultrasound. Nanofluids made it possible to increase the collector efficiency by 23.3% compared to the base fluid. The optimum particle concentration was 0.005 wt%. and the flow rate was 0.015 kg/s. The thermal efficiency of a collector with nanofluid reached 93% when the temperature on the inlet of the collector was equal to the temperature of the environment.

Li et al. [27] consider a solar collector using water-based nanofluids and nanofluids based on Terminol 55 with multi-walled carbon nanotubes. The nanotubes were functionalised with potassium persulfate. The design of the collector is notable as a low-profile concentrating tubular model is considered. Interesting experimental results were obtained in the study. A solar collector using nanofluid as a volumetric absorber demonstrated lower thermal efficiency than a collector with blackened absorber tubes (black chrome receiver) and the base fluid. The efficiency of the nanofluid-based collector was lower by 14%...21%. According to the authors, one of the reasons for this result is that DASC had higher heat losses due to the high emissivity of the absorber surface and the absence of an anti-reflective coating.

Gorji and Ranjbar [28] presented the efficiency study of a lab-scale DASC. Three types of aqueous nanofluids with silver, magnetite, and graphite particles were used as working fluids. The collector was irradiated with artificial thermal radiation using a halogen lamp. As a result of the tests, the use of nanofluids instead of water leads to an increase in the thermal efficiency of the collector up to 90%, while the efficiency of the water-based collector for the same flow parameters show only about 30%.

A flat direct absorption collector using a nanofluid with gold particles was described in the work [29]. The nanofluid was synthesised by a chemical method from an aqueous solution of chloroauric acid. It was found that the use of nanofluid increases the thermal efficiency of the DASC collector up to 31% compared with the case of using pure water as a working fluid.

Many of the reviewed studies that presented the advantages of nanofluids in DASC did not compare energy absorption in nanofluids with opaque/blackened surfaces but in comparison to the nanofluid-DASC case with the DASC with the transparent base fluid. It is obvious that a "colored" fluid absorbs more heat. The presented studies also show that the efficiency of DASC depends mostly on several factors: the type and concentration of particles, the flow rate, and the temperature difference between the fluid and the environment. The combinations of these factors and their influence on the thermal efficiency of DASC are not thoroughly studied in the mentioned contributions.

In the present work, we consider the effect of a wide range of the process parameters and their combination on the thermal efficiency of DASC with nanofluid based on multi-walled carbon nanotubes (MWCNT) and we compare them with the cases when an equally-sized opaque receiver is used. In addition, our work is aimed at a detailed theoretical description of the prototype using a multiphase CFD model that provides insight into flow patterns and describes how the nanoparticles deposit in the collector. We validate the model with the produced experimental data.

2. Experiments

2.1. Nanofluid

In this study, the nanofluid consisted of multi-walled carbon nanotubes (MWCNTs) dispersed in a water-ethanol base (10%wt.) used to enable operation of DASC at ambient temperatures down to -6°C. The selected minimum temperature corresponds to mid-season conditions in northern countries. The nanotubes were stabilised in the base using 0.1%wt. sodium dodecyl sulfate (SDS). The use of SDS is a simple and well-studied method for stabilising carbon-based nanofluids [30, 31]. The nanofluid was protected from the formation of foam using 0.4%wt. of a commercial defoamer "FoamStop" from Kärcher.

The nanotubes at concentrations 0.0015...0.082% were dispersed in the base using the two-step method. The commercial MWCNTs Dealtom were purchased from Nanotechnology Center (Moscow, Russia) [32]. The inner diameter of nanotubes is 13.3±0.45 nm, and the external diameters are 49.3±0.45 nm or 72.0±0.45 nm. A rough estimate of maximum length is 5 μm. The microscopic images of the tubes obtained by means of scanning electron microscopy (SEM) are presented in Figure 1.

We produced the nanofluid in several stages. At first, the required mass of the dry nanotubes was mixed with the distilled water, ethanol, and SDS and then sonicated for 1 hour in an ultrasonic bath VBS-27D from Vilitek at 600 W and 40 kHz. The nanoparticles and the surfactant were dosed with accuracy ±1 mg using the FC-50 analytical scale. After the ultrasonic treatment, the defoamer was dissolved in the nanofluid by gently shaking the sample. The full load of our DASC was 9 kg, so the respective batch of the nanofluid was produced for each particle concentration. Further,

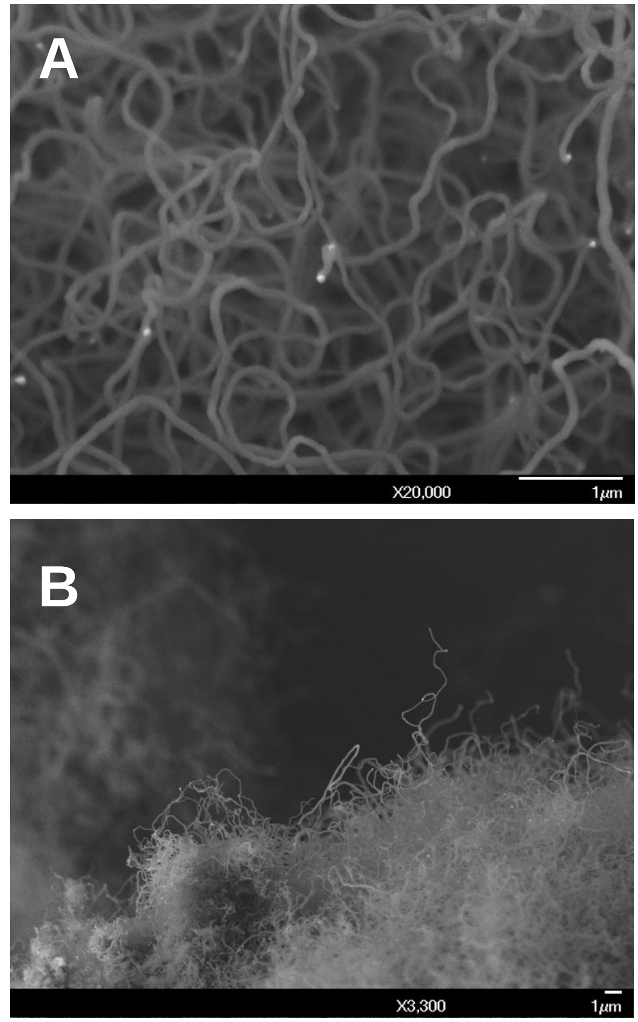

Figure 1: SEM images of multi-wall carbon nanotubes Dealtom (RPE "Nanotechnology Center") with x20 000 (A) and x3 300 magnification (B)

the nanofluid was kept in a static condition for 24 hours for the gravitational separating of non-Brownian agglomerates. After separation, the nanofluid was gently poured over to an empty tank, and the deposit of particles was left in the contaminated vessel. Drying the deposit we obtained the mass of the settled particles and re-calculated the concentration that was left in the nanofluid.

In Fig.2 we present how the final concentration of the nanoparticles x_f depends on the initial concentration x_{in}. We read from the figure that there is a linear dependence between the initial particle concentration and the concentration after separation. The average fraction of the deposited particles was 60±10% for the considered initial concentrations. In addition, we studied how the amount of surfactant affects the deposition. It was observed that the fraction of the deposited particles decreased when the ratio of the mass of

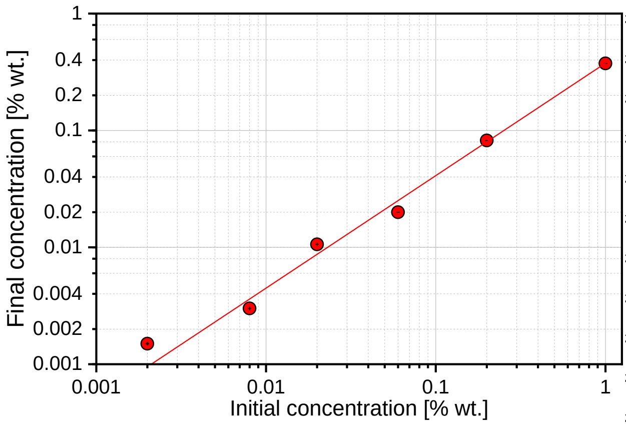

Figure 2: Evolution of nanoparticle concentration due to settling for different initial MWCNT concentrations

the surfactant to the mass of the particles m_{SDS}/m_{MWCNT} is increased. According to obtained results, 48...60% of deposited particles are observed at m_{SDS}/m_{MWCNT}<12.5. This number reduces to 20% at m_{SDS}/m_{MWCNT}=50.

Despite the positive effect of increasing the SDS ratio and particle mass shown in this study, it is worth noting that an optimal range of surfactant concentration exists. Low SDS concentrations do not provide enough molecules to build spatial structures around graphene particles that reliably prevent agglomeration. At high concentrations of SDS, the process of micelle formation is activated, leading to the agglomeration of SDS molecules attached to the particles and, respectively, bridging the particles [30]. According to our estimates, the formation of micelles in the nanofluids of the present composition must be observed at SDS concentrations above 0.17% wt.[33].

The produced nanofluids demonstrated stability at least six months after experiments: the nanofluid bulk remains homogeneous, without visible stratification. The samples of nanofluids at different MWCNT concentrations are depicted in Fig.S1 of the Supplementary Materials. A small deposit of particles was formed in nanofluids with relatively high concentrations (0.020%, 0.082%) after about a month in static condition.

As mentioned above, the optimum concentrations of surfactants exist. At this concentration, the nanofluid maintains the least possible agglomeration of particles. The optimum concentration of SDS depends on the type and concentration of particles and the type of base fluid. Thus, taking into account the value of the critical micelle concentration for our nanofluids and the desire to keep the surfactant mass higher than the particle mass for reliable absorption at the particle surface, we set the concentration of SDS equal 0.1%.

The characterisation of the developed nanofluids included the analysis of *in-situ* particle size distribution. Fig. 3 shows the DLS-analysis results performed using Malvern Zetasizer Nano ZS. The scattering light (He-Ne laser, 632.8 nm) was collected at a 173° scattering angle at 25 °C. The samples were studied less than 24 hours after the deposits were removed from the nanofluid. As can be seen in Fig. 3, the average size of agglomerates almost independent of concentration and just slightly increases with the growth of particle concentration. The average size of agglomerates is in the range 209...230 nm.

In supplementary tests, the transmittance of nanofluid layers of variable thickness was studied for two wavelength ranges 400...1100 nm and 1000...1700 nm. The measurement of the light absorption was carried out for the freshly prepared nanofluids. The details of the experiment are presented in the Supplementary Materials (see Figs.S.2-S.3). Basing on the measured transmission, we determined that the extinction coefficient κ_{nf} varied in the range 220...1255 m^{-1} for the experimental MWCNT concentrations. The extinction coefficients for different initial mass fractions of the particles are presented in Table 1. In the table, they are shown separately for two parts of the spectrum: 400...1100 nm (I) and 1100...1700 nm (II).

x_{in} [%]	0.000	0.008	0.010	0.020	0.050	0.100
$\kappa_{nf,I}$ [1/m]	25	220	201	522	709	1222
$\kappa_{nf,II}$ [1/m]	161	378	401	664	804	1255

Table 1: Extinction coefficient of the nanofluids

2.2. Direct absorption solar collector

The nanofluid was tested in a lab-scale prototype DASC of tubular type. The experimental rig is schematically presented in Fig. 4.

The system included the DASC, which consisted of 8 glass tubes connected in series. The tubes were made of borosilicate glass 3.3 "SIMAX", ∅22 × 1.8 mm, the length of the tubes is 1500 mm. The tubes were connected using seven 180° copper bends. The distance between the axes of the tubes is 35 mm. The DASC was mounted at a rectangular frame with a total area of 0.49 m^2. The frame was inclined by an elevation angle of 45°. An insulating bed of ceramic fibre with the thermal conductivity of ≈ 0.2 W/(m·K) was mounted on the frame. The bottoms of the glass tubes were

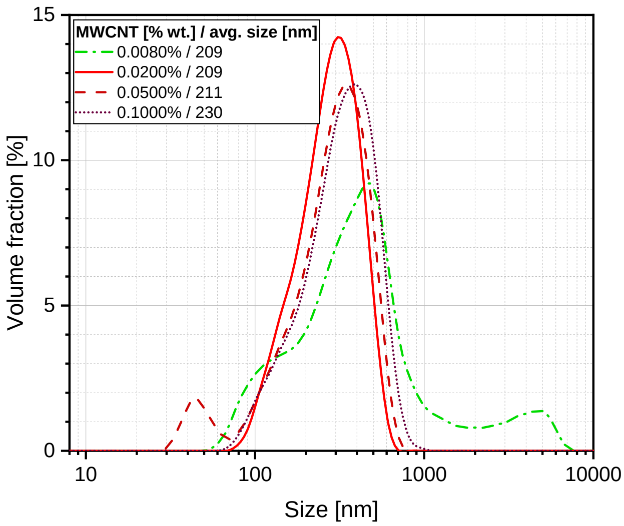

Figure 3: Particle size distribution for different concentration of MWCNTs in nanofluid

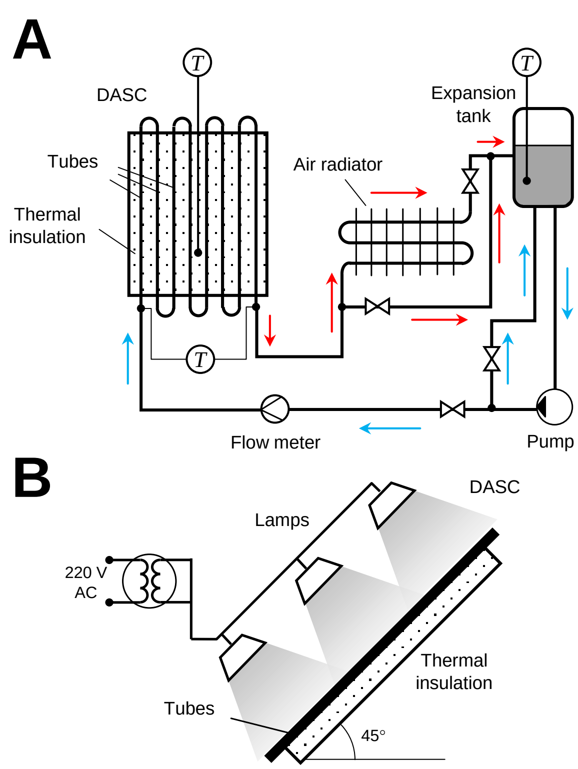

Figure 4: Schematic image of the direct absorption solar collector. Front view (A) and side view (B)

immersed into the fibre. The centrifugal pump Multi 14000E from Sicce with a closed impeller was used for pumping the nanofluid. The air-cooled tubular heat exchanger Luzar LRc 01080 with a fan regulated by pulse-width modulation was used for cooling the nanofluid after its heating in DASC. The experimental rig was located in a hermetic pallet to avoid possible nanofluid leaks to the environment.

During the experiments, the temperatures of liquid and ambient air were measured by K-type thermocouples connected to the digital thermometer Center 309 (0.1 °C, ±(0.3% + 1 °C)). The nanofluid heating was measured by a custom-made differential T-type thermocouple connected to an APPA 207 multimeter (1 μV, ±(0.06% + 2 μV)). The calibration dependence of the differential thermocouple was obtained in separate tests. The thermocouple's beads were soldered into the wall of the brass fittings placed at the inlet and outlet tubes of the collector. The rotary flowmeter YF-S201 (0.07 l/min, ±10%) was used to control the flow rate. The flowmeter was connected to Arduino digital plate and calibrated in separate tests. Three halogen lamps (Osram Haloline Pro, 400 W) were used for the simulation of radiate heating at an area-average light flux of 915 W/m^2 and 500 W/m^2. Before averaging, the spatial distribution of thermal radiation was measured by LS 122 IR from Shenzhen Linshang in fifteen points by length for each glass tube. The units of the rig were inter-connected by flexible hoses, which were insulated thermally by polyurethane foam with the thermal conductivity of ≈ 0.03 W/(m·K).

The experiments aimed to determine the positive temperature difference over DASC (i.e. heating of the fluid) for an altering flow rate (2...10 l/min), MWCNT concentration, irradiation, and temperature drop between the DASC and environment. In addition, to compare with a standard case of surface absorption, we conducted a test when the tubes were coated with black matt aluminum foil. Distilled water was used in the opaque system along width a reference test with transparent tubes.

The experiments were carried out in several steps. We filled the entire flow loop with nanofluid of the required concentration. The forced circulation of the liquid started at the maximum flow rate of 10 l/min; the lamps were switched on the full power simultaneously. The stabilisation of the set-up to a thermal steady-state condition began after the liquid was $10°C$ warmer than the environment. The stabilisation was achieved by steering the fan and the flow through the radiator via the by-pass line. The temperatures and the flow rates were recorded after the thermal stabilisation. The data was recorded for 5-10 minutes. The next measurement was done by reducing the flow rate incrementally by 2 l/min, altering the cooling to set the same temperature difference, and waiting for the new steady-state condition. The equivalent series of experiments were run for the temperature differences of

$20°C$ and $30°C$. Then the pump and the lamps were turned off, and the set-up cooled down to the ambient temperature. After the cooling, the lamp power was decreased, and the described measurements were repeated. At the final stage of the experimental set, the set-up was emptied and cleaned. The cleaning procedure is described below. A new nanofluid with another concentration was further charged in the rig and underwent the same procedures.

An important parameter that characterises the performance of solar collectors is thermal efficiency. Following the standard methodology described in Duffie [34], the thermal efficiency was determined as the ratio of the absorbed thermal power in the DASC to the radiated power at the surface of the tubes of the test section:

$$\eta_{nf} = \frac{\dot{m} C_p \Delta T}{GA}, \tag{1}$$

where $\dot{m}$, C_p, ΔT are the mass flow rate, specific heat and the heating of the fluid, G is the irradiation with A as the irradiated area of glass tubes. Due to the low number of nanoparticles, the equivalent thermal properties of the nanofluid were set as for the base fluid and were taken from [35, 36]. This simplification corresponds to the third-party experiments on the characterisation of thermal properties of MWCNT-based nanofluids [37–39]. In our work, the concentrations of nanoparticles are low and so the modification of properties in negligible.

3. CFD model

A supplementary multiphase CFD model of the experiment was developed to provide better insight into flow patterns and estimate the deposition of nanoparticles in the flow system. The model was built using the commercial CFD package STAR-CCM+ from Siemens (v.13.06.012) whose standard multiphase two-fluid Eulerian model was extended in-house.

3.1. Mesh and boundaries

The geometry of the model reproduces the entire tubular section of DASC. The geometry was discretised in the radial direction using 3.4 mm^3 polyhedral control volumes. The computational mesh is presented in Fig.5. To set Y+<1, as required by the turbulence model, the mesh was refined near walls with a 0.15-mm thick subsurface consistent with 6 layers of prism cells. The grid of the straight tubes was coarsened downflow via 3-mm anisotropic stretching of the cells. There were about 1 770 000 cells in the model.

The mesh size was determined after the mesh-sensitivity analysis using twice finer and 80% coarser grid sizes. The finer mesh resulted in a ~4% average discrepancy of the main flow patterns relative to the present case but with a significantly higher wall time. The coarser mesh deviated by about 11%. The boundary conditions included the standard inlet with the prescribed velocity, volume fraction, turbulent properties, and temperature. The pressure outlet set zero gradients of volume fraction and temperature. The no-slip boundary condition was used at the walls together with the standard wall functions of the k-epsilon turbulence model.

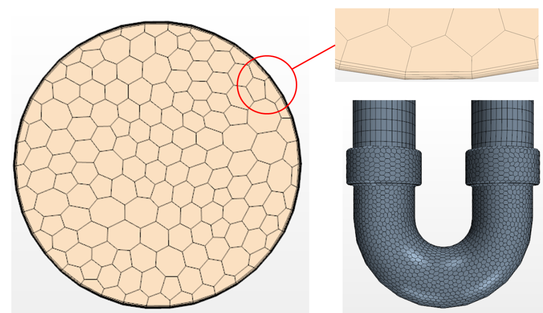

Figure 5: Computational mesh

The thermal condition at the wall was complex and depended on two simulated alternatives: opaque black tubes or volumetric absorption in transparent DASC. The top half of the tubes is subjected to thermal radiation and returns heat to the environment. Several thermal leaks are incorporated in the model: a reflection from the pipes, convective and radiate thermal loss to the air. The reflection was determined experimentally as 10% for the opaque tubes and 5% for the transparent tubes. The radiation from the collector was modeled as in Bårdsgård et al. [40] via Stefan-Boltzmann's law with emissivity of 0.8 and 0.96 for the opaque and transparent cases, respectively. The coefficient of heat transfer for natural convection of air at an inclined surface is computed following Rohsenow et al. [41]. This method is cumbersome. We present it in the Supplementary Materials.

The bottom part of the tubes is considered adiabatic for the opaque case. This condition is not entirely valid when the radiation penetrates the fluids and meets the thermal insulation. In this case, as determined experimentally, 55% of the flux is reflected back to the fluid. The rest is accumulated in the insulation layer, which is again set as a heat flux condition at the bottom half of the transparent DASC.

Another important detail of the process is the temperature of the surrounding air, which is not constant along the collector. As derived from our thermal analysis, the convective layer of air is formed in the gap between the lamps and the top surface of the tubes. The lamps and the associated frames formed an additional aerodynamic resistance driving the air along the tubes. The resulting ambient temperature at the top of the collector was about 3°C higher than the value measured at the sensor. In experiments, the sensor was located in the gap between lamps and tubes, at the lower third of the collector's length. Therefore, the ambient temperature in the model was presented by the linear interpolation between the control point and the top of the DASC.

3.2. Model description

The nanofluid is modelled following the formulation of Gidaspow's Model A [42] where two inter-penetrating fluids sharing the same pressure are described by two separate systems of Navier-Stokes equations. The continuity reads [40]:

$$\frac{D(\alpha_i \rho_i)}{Dt} = 0, \tag{2}$$

where $D../Dt$ is the substantial derivative, α_i and ρ_i are the volume fraction and the density of ith phase, $i = p$ stands for particles and $i = l$ for base fluid; α_l+α_p=1.

$$\frac{D(\alpha_i \rho_i \mathbf{v}_i)}{Dt} = -\alpha_i \nabla p + \alpha_i \left(\mathbf{T}_i + \mathbf{T}_i^t\right) + \\ + \alpha_i \rho_i \mathbf{g} + \mathbf{M}_{i,j} + \delta_{i,p} \mathbf{F}_{th}, \tag{3}$$

In Eq.3 $\mathbf{v}$ is the velocity, $\mathbf{T}$ and $\mathbf{T}^t$ are the tensors of molecular and turbulent stresses, p is the pressure, $\mathbf{g}$ acceleration due to gravity, and $\mathbf{M}_{i,j}$ is the superposition of drag $\mathbf{F}_{D,ij}$ force, added mass force $\mathbf{F}^{vm}_{i,j}$, and lift force $\mathbf{F}^{L}_{i,j}$. The molecular stress tensor in the particulate phase is computed using the base fluid viscosity, which is a reasonable assumption for low concentrations of particles used in the experiments. It is also confirmed experimentally by Hamze et al.[43] for homogeneous dispersions of MWCNTs in water. The turbulent stress is computed in the base fluid for Re>4000 using the k-epsilon model, and there was also simulated a laminar case for Re=2380. The turbulent viscosity in the particulate phase is obtained using the turbulent response concept via the respective parameter of the base fluid $\mu_p^t = \rho_p/\rho_l \mu_l^t$.

A phenomenon that is important in the flows with nanoparticles is the Brownian motion [44]. The process results in thermophoresis when sufficient temperature gradients are formed in the flow. Using expressions from the detailed review by Sager [45], we estimated that the momentum of nanoparticles due to thermophoresis was at least 5 orders larger than the motion of the particles due to collisions caused by Brownian dispersion, i.e. the Brownian diffusion. Therefore, in the present numerical approach, we assumed Brownian diffusion is negligible and model thermophoresis via the respective expression $\mathbf{F}^{th}$, which is applied solely to the particulate phase using the Kronecker's function $\delta_{i,p}$. Another important remark follows from Michaelides [44] who mentioned that turbulent diffusion adds 30% to the deposition of particles above 100 nm. Therefore, we include turbulent dispersion force $\mathbf{F}^{td}_{i,j}$ to $\mathbf{M}_{i,j}$.

The forces are given per unit volume of nanofluid scaling a single-particle force by the number density of nanoparticles n_p within a computational cell:

$$\mathbf{F}_{D,ij} = \frac{\pi d^2}{8} n_p \rho_l C_D C_f C_c^{-1} \mid \mathbf{v}_i - \mathbf{v}_j \mid \left(\mathbf{v}_i - \mathbf{v}_j\right), \tag{4}$$

where d is the size of the nanoparticles and C_D is the drag coefficient computed using the standard expression by Schiller-Naumann [46]. The rarefaction of the continuous phase at the nanoparticle scale is accounted for by Cunningham's correction [46]:

$$C_c = 1 + \mathrm{Kn}(2.49 + 0.85\exp[-1.74/\mathrm{Kn}]), \tag{5}$$

where Kn is Knudsen's number for the nanoparticles. Following Fuchs [47], we introduce the statistically-average form-factor C_f=0.66 to account for an ellipsoid-like shape of the particles.

The added mass term is given by [48]:

$$\mathbf{F}^{vm}_{ij} = C^{vm} \rho_l \alpha_p \left(\frac{D\mathbf{v}_i}{Dt} - \frac{D\mathbf{v}_j}{Dt}\right), \tag{6}$$

where C^{vm}=0.5 is the virtual mass coefficient.

The lift force is computed as follows [48]:

$$\mathbf{F}^{L}_{ij} = C^{l} \rho_l \alpha_p \left(\mathbf{v}_i - \mathbf{v}_j\right) \times \left(\nabla \times \mathbf{v}_l\right), \tag{7}$$

where C^l=0.25 is the lift coefficient [49].

The turbulent dispersion force depends on the turbulent diffusivity of the nanoparticles $D^{td} = \mu_l^t/(\rho_l \sigma_l^t)$ with turbulent Prandtl number σ_l^t=0.9 [50]:

$$\mathbf{F}_{ij}^{td} = \frac{3\alpha_p \rho_l C_D}{4d} \mid \mathbf{v}_i - \mathbf{v}_j \mid D^{td} \cdot \left(\nabla \ln \alpha_i - \nabla \ln \alpha_j\right) \quad (8)$$

The thermophoretic force $\mathbf{F}_{th}$ is given by [51]:

$$F^{th} = \frac{-6n_p \pi \mu_l \nu_l d C_s}{1 + 6C_m \mathrm{Kn}} \frac{k_l/k_p + 2C_t \mathrm{Kn}}{1 + 2k_l/k_p + 4C_t \mathrm{Kn}} \frac{\nabla T_l}{T_l}, \quad (9)$$

where k_i is the thermal conductivity, ν_l is the kinematic viscosity of the liquid, and the coefficients are $C_s = 1.17$, $C_t = 2.18$ and $C_m = 1.14$ [46].

The energy equation is given as [52]:

$$\frac{D\left[\alpha_i \rho_i \left(e_i + 0.5 \mid \mathbf{v}_i \mid^2\right)\right]}{Dt} = -\alpha_i \nabla \cdot \left(p \cdot \mathbf{v}_i\right) + \alpha_i \rho_i \mathbf{v}_i \cdot \mathbf{g} + q_{ij}$$
$$+ \alpha_i \nabla \cdot \left(\left[\mathbf{T}_i + \mathbf{T}_i^t\right] \cdot \mathbf{v}_i\right) + \alpha_i q_v + \alpha_i \nabla \cdot \nabla \left(k_{eff,i} T_i\right) \quad (10)$$

In Eq.10 $e_i = C_{p,i} T_i$ is the enthalpy, the effective thermal conductivity of the phase is computed as $k_i + \mu_i^t C_{p,i}/\sigma_i^t$. The inter-phase heat transfer source term is given by Ranz-Marshall expression [46]. The thermal properties of the phases in Eqs.3 and 10 were set for each phase separately. The base fluid was defined as in [35, 36]. The thermal conductivity of the nanoparticles was taken from Zhang et al.[53] and the specific heat from Yi et al.[54]. In the simulations, we did not additionally customise the equivalent thermal properties of the nanofluid as they were not modified significantly due to the low content of nanoparticles used in the experiments.

The volumetric heat generation term q_v represents the volumetric absorption of thermal radiation. The source term depends on the nanofluid extinction coefficient κ_{nf} following Beer-Lambert's law:

$$q_v = \frac{d}{dl}\left(I \exp\{-\kappa_{nf} l\}\right), \quad (11)$$

where I is the superposition of the heat flux from the top surface of the tubes $I_t = r_t G$, where r_t is the reflectance of the top surface, and the radiant heat reflected from the bottom (denoted as b) of the tube with the diameter D_p: $I_b = r_t r_b G \exp\{-\kappa_{nf} D_p\}$. The coordinate l is the lightpath in the respective direction.

A simplified correlation is developed for the extinction coefficient of the nanofluid using the experimental data from Table 1. Following Taylor et al.[55], the efficiency of extinction is given by the sum of the absorption efficiency and the scattering efficiency. The latter is an order of magnitude smaller. When combined in the extinction coefficient, both terms are proportional to the volume fraction of the nanoparticles, while the second term is also dependent on d^3. Therefore, we fit the average extinction coefficient, obtained experimentally, as:

$$\kappa_{nf} = \kappa_f + \frac{3}{2}\alpha_p \mathcal{A}\left(1 + \frac{d^3}{\mathcal{B}}\right), \quad (12)$$

where κ_f is the average extinction coefficient of the base fluid (determined experimentally) and $\mathcal{A}$=2.3·10^6 m^{-1} and $\mathcal{B}$=10 m^3 are the fitting constants.

The governing equations were discretised in space using the upwind scheme. The temporal discretisation was done using the second-order Euler implicit technique with a time step of 10 ms. The equations were solved numerically using SIMPLE with the following relaxation coefficients: 0.7 velocity, 0.8 turbulent model, 0.3 pressure, 0.9 enthalpy, 0.5 volume fraction. The simulations were considered convergent when the residuals dropped below 10^{-5}. In addition, we monitored the main process parameters: the thermal efficiency, the pressure drop, the volume fraction, and the values of Y+ that were always below unity. These monitors reached a steady-state when the simulation converged.

The proposed modelling approach including the combination of the multiphase Eulerian model with the k-epsilon model does not demand high computational costs and becomes suitable for simulation of photothermal phenomena at a device scale. In this study, we ran the simulations using 25 cores INTEL(R) Xeon(R) W-2195 CPU @ 2.30 GHz.

4. Results and discussion

4.1. Experiments

At first, it is important to compare how the volumetric absorption of thermal radiation differs from the surface absorption in our system. In Fig.6A, we demonstrate how the temperature difference between the outlet and the inlet from the DASC depends on the flow rate in case water is used in the collector. As expected, the heating of the fluid reduces with the flow rate due to reduced residence time in the collector. The heating of water in transparent channels is lower than in blackened ones due to the lower amount of absorbed energy in the system: both uncoated glass and water are weak absorbers of light energy. In contrast, a black, opaque surface absorbs more heat when exposed to light and transfers heat to water through a combined action of thermal conduction and forced convection. Further, the plot of Fig.6B presents how the nanofluid with 0.01% wt. MWCNT is heated for the equivalent flow rates. The nanofluid becomes warmer by 9...27% compared to in the opaque and transparent case. Nevertheless, the general tendency of decreasing liquid heating with an increasing flow rate persists.

The concentration of nanoparticles also affects the heating of the nanofluid in the collector. It is clearly seen in Fig. 7, which also shows the existence of the optimum concentration. At this concentration, the maximum temperature is gained by the nanofluid at the same flow rate and irradiation. As will be shown below, the optimal particle concentration in our study was 0.01%. The nanofluid absorbs more thermal energy than the opaque receiver due to the difference in the temperature profiles at the irradiated surface. The opaque receiver transfers the absorbed heat to the working fluid due to thermal conduction within the wall and convection from the wall to the liquid. There must be a considerable temperature gradient between the receiver and the liquid, so the temperature of the receiver is relatively high compared to the bulk of the liquid. This means that the thermal leaks from the opaque system are significant.

In DASC, the radiated heat is absorbed mostly on the particles' surface and less by the carrier fluid. In this case, heat is transferred from the overheated particles directly to the base fluid, skipping the conduction stage in the collector's wall. The surface of the collector is colder which drops the thermal loss to the environment. It is also confirmed by the performance analysis of the DASC shown in more detail in Fig.8. This figure shows the dependence of the collector's thermal efficiency on the particle concentration and the volumetric flow rate of nanofluids for four groups of experiments. The groups differ by the irradiation and the temperature drop between the environment and the inlet of the collector.

Fig. 8 illustrates that for MWCNT concentrations above 0.003% the nanofluid sets sufficiently higher efficiency than the opaque surface. The highest efficiency in the range 0.80...0.97 was achieved with a 0.01% wt. nanofluid. It is 5.8...37.9% higher than for the opaque receiver.

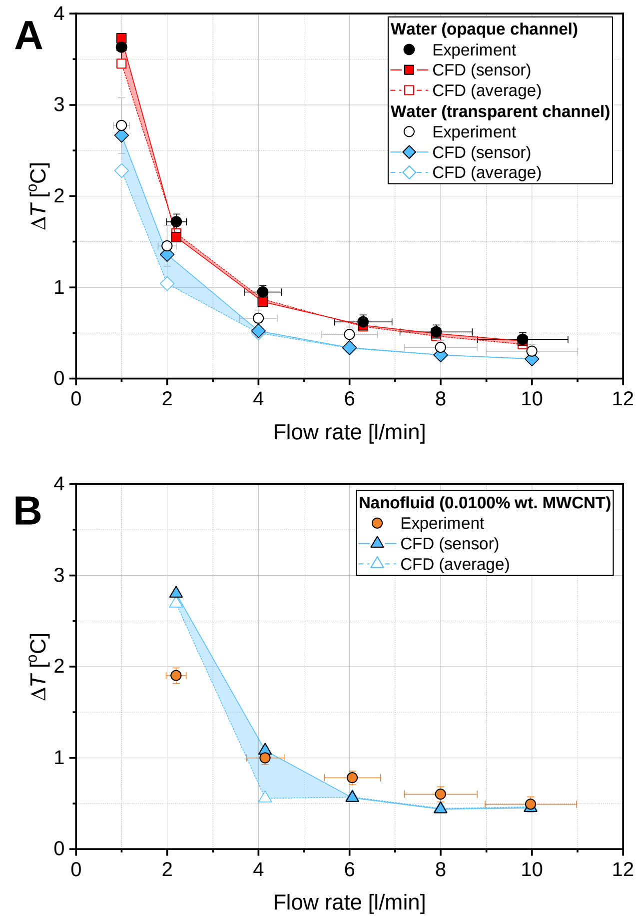

Figure 6: The temperature difference between outlet and inlet of the DASC with water (A) and nanofluid (B) for different flow rates and optical conditions at $G = 915$ W/m^2. The concentration of nanoparticles was 0.01 %wt.

The advantage of DASC becomes more significant with an increase in the temperature drop between the liquid and the environment. For the case when T_i-T_a=20 °C, the nanofluid of optimum composition delivers 25...35% more heat than the opaque solar collector. However, we note that the nanofluid-based DASC reduces the efficiency by 5% and 25% when the temperature drop increases by 10 °C and 20 °C, respectively.

The thermal efficiency is proportional to the flow rate, increasing by 10...15% when the flow goes from 2 to 10 l/min at irradiation of 915 W/m^2. It is interesting to observe that the efficiency drops at reduced irradiation (G = 500 W/m^2) in the nanofluid-based DASC for the maximum flow rate 8...10 l/min. At the same time, the opaque system demonstrates a continuous increase of efficiency with the flow. The appearance of the optimal flow rate in DASC is explained as follows. In DASC, nanofluid is the main absorber of light

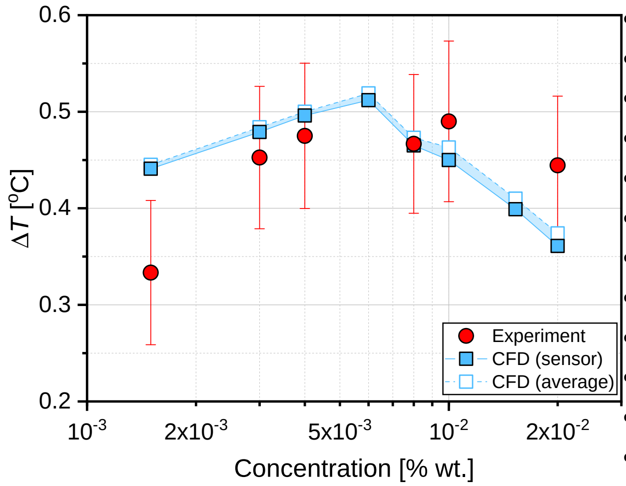

Figure 7: The temperature difference between outlet and inlet of the DASC for different concentrations at 7.9 l/min and $G = 915$ W/m^2.

energy, which leads to its overheating relative to the transparent wall. Therefore, a decrease in the flow rate below the optimal value increases the irradiation time of the particles in the frontal layers of nanofluid and their superheating. On the opposite, an increase in the flow rate intensifies the heat transfer between the wall and the liquid. Both cases lead to increased heat losses. In a collector with a blackened absorber, the heat absorbed on its surface is directed either into the liquid or the environment. Therefore, an increase in the flow rate of the fluid and the intensity of heat transfer will increase the part of the heat that goes into the liquid and, as a result, continuously increase the efficiency. Out of this observation we conclude that the optimum set point of DASC results in a notably lower pumping cost which is another advantage of the proposed system.

The effect of particle concentration on the DASC thermal efficiency is shown in Fig. 9. The figure presents the thermal efficiency, averaged over the entire range of flow rates for every studied concentration of particles.

Fig. 9 confirms that an optimum concentration of nanoparticles exists. At this concentration, the thermal efficiency of DASC is maximum. The optimum concentration was 0.01% wt., which allowed for obtaining a the thermal efficiency up to 96.7%. The effect of concentration on thermal efficiency is explained as follows. At low concentrations, the nanoparticles do not provide much surface to absorb incident radiation in bulk and total amount of absorbed energy in fluid is low. However, increasing the concentration over the optimum, the system gets into conditions when the radiation is absorbed in a thin layer of fluid adjacent to the outer surface. Therefore, the DASC asymptotically approaches the opaque case with surface absorption which is characterised by the noticeable overheating of the absorber surface relative to the ambient and, as a consequence, higher heat losses. This also correlates with the data obtained for the heating of nanofluids, shown in Figure 7.

We also note that the nanofluid with concentration 0.082 % wt. deviates from the described qualitative behaviour for the group with the maximum temperature drop. We address this observation to a partial destabilisation of the nanofluid at this relatively high initial concentration. The deposits originating from the unstable nanofluid formed a semi-opaque environment with reduced MWCNT concentration in bulk, resulting in a relatively high thermal efficiency. However, this efficiency was not over the maximum value at the optimum concentration.

The thermal efficiency of our DASC was compared in Fig.10 with the third-party studies of the nanofluid-based DASCs and the efficiency of commercial solar collectors with the opaque receivers. A flat collector with the selective coating [56] (Moscow, Russia) and a vacuum tube collector with heat pipes [57] (Warwick, USA) were chosen as the commercial models.

Fig. 10 shows that DASC with carbon-based nanofluids has the highest thermal efficiency, which can be explained by the better absorbance of the carbon material. The selected commercial collectors generally have better performance than the third-party DASCs with nanofluids which possess a rather simplistic thermal design. The third-party results show that, in general, our DASC returns up to 55.8% higher thermal efficiency.

Several reasons can lead to this result. The first is the tubular design of the collector, so it was possible to arrange for the reliable thermal insulation of every tube. In other studies, a flat fluid compartment was chosen, often without thermal insulation. An exception is the study by Li [27], where a tubular concentrating collector with reflectors was used. The thermal efficiency of this collector is comparable and, in several cases, exceeds the efficiency of our DASC. Another reason is the use of a higher flow rate in our work, while in other studies, the nanofluid flow rate did not exceed 1.5 l/min. The simultaneous use of tubular channels and the increased flow rates leads to higher Reynolds numbers and, consequently, to better turbulent mixing in the flow. In our case, the nanoparticles heated at the top surface will swiftly

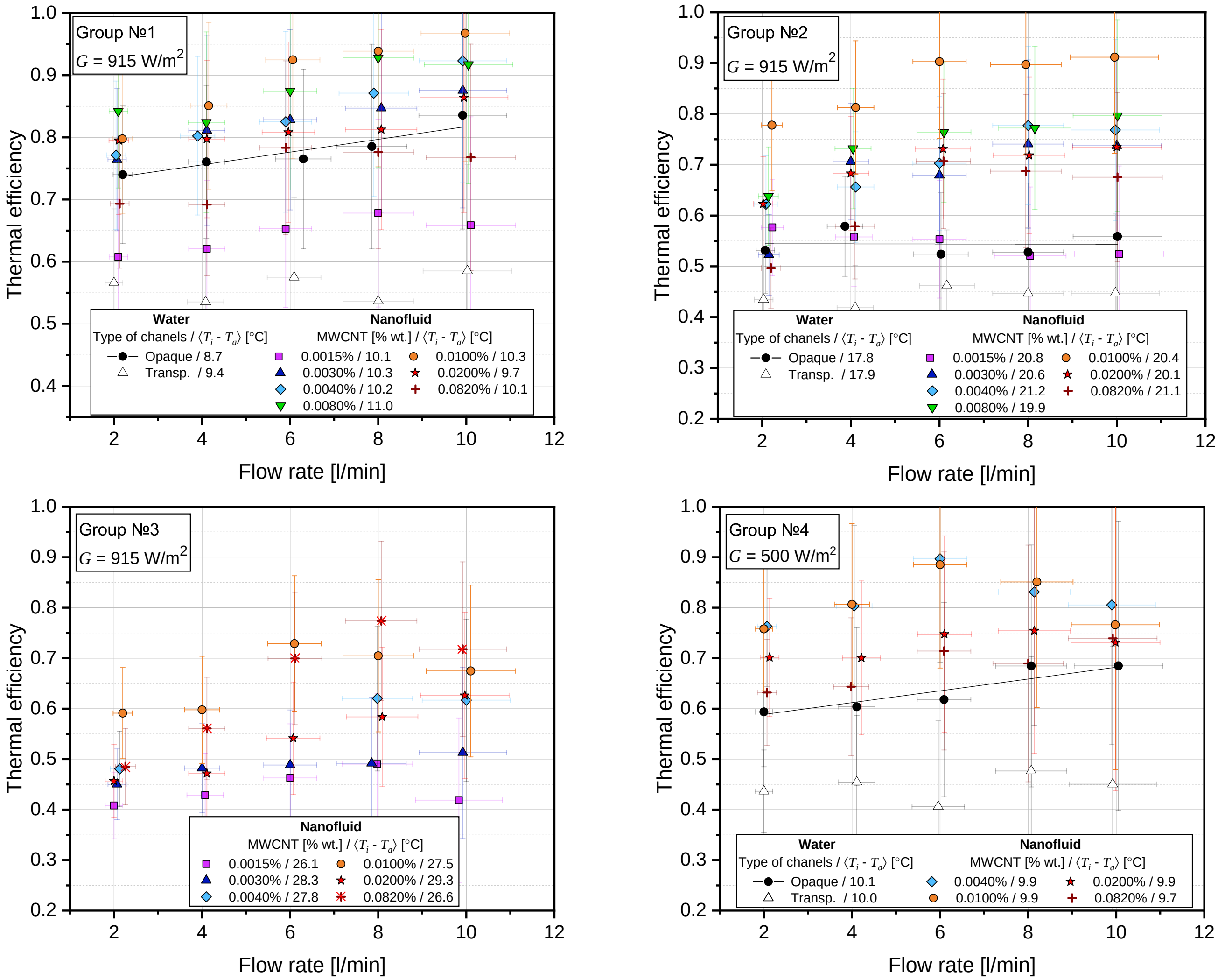

Figure 8: The thermal efficiency of DASC for different MWCNT concentrations, flow rates, temperature drops, and optical conditions

move into deeper layers, providing a more uniform heating of the receiver. On the contrary, low flow rates in wide flat channels do not intensify particulate dispersion in the flow. It leads to larger temperature gradients in the liquid and increases the thermal leaks.

The optimum concentration of particles in the third-party experiments with carbon-based nanofluids is in the range of 0.005...0.1%wt. Therefore, the optimum particle concentration detected in our study is consistent with other works. The observed range of variation of the optimum concentration is most likely associated with the different shapes and sizes of particles and different geometry of the collector channels, affecting both the temperature distribution in the liquid and the heat losses to the environment.

Comparing the thermal efficiency of our DASC with the commercial collectors, we demonstrate that the efficiency of our system is up to 20% better than for the vacuum tube type collector and up to 25% higher than for the flat-plate collector. However, our DASC performs better than the commercial collectors in a rather narrow temperature drop range, namely below 30 $°C$. When approaching this value, the DASC thermal efficiency becomes comparable with the selected commercial models. We address this issue to a less than optimum thermal insulation of the top surface and the lack of anti-reflective coating used in the commercial models.

At the end of the analysis, it is essential to note that the hydraulic resistance of our DASC is low. The pumping cost at the maximum experimental flow rate deducts only 0.2% from the total efficiency of the system.

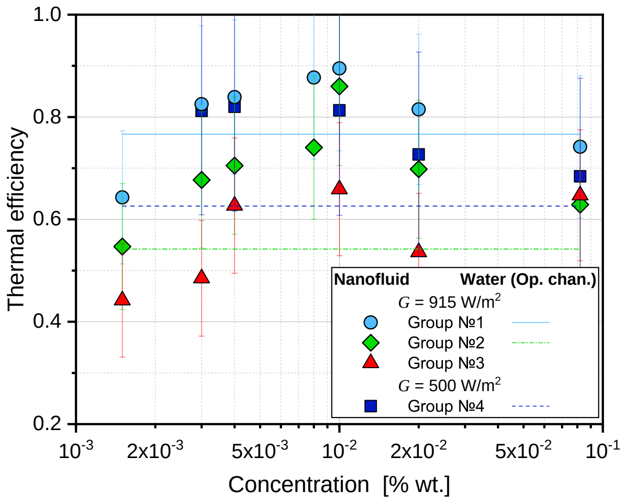

Figure 9: The thermal efficiency of DASC averaged within the range 2...10 l/min for different particle concentrations.

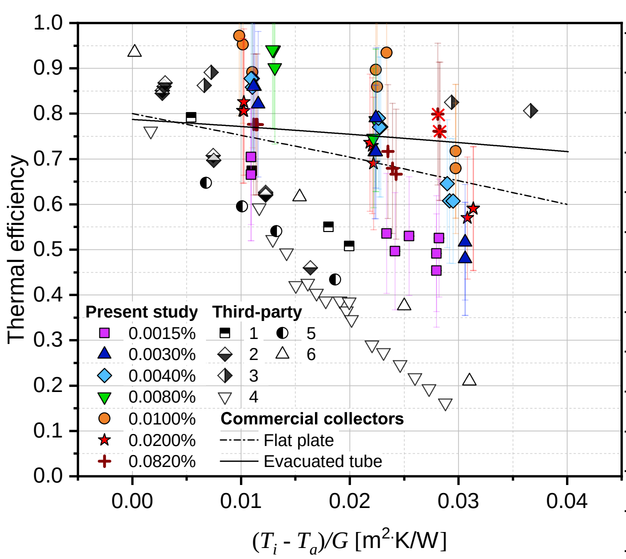

Figure 10: Efficiency grade plots for DASCs and commercial solar collectors. Third-party experiments: 1. Delfani et al. [25] (MWCNT, 1.34% wt.), 2. Vakili et al. [26] (graphene, 0.005% wt.), 3. Li et al. [27] (MWCNT, 0.005% wt., vacuum), 4. Gupta et al.[23] (Al_2O_3, 0.02% wt.) , 5. Karami et al. [24] (CuO, ≈1.45% wt.), 6. Kumar et al. [29] (gold, 0.0002% wt.).

4.2. Notes on the operation of DASC

The developed fluids are easy to produce and of a rather simplistic composition. Our nanofluids are manufactured at a moderate cost of about 2.6 \$/kg. The nanofluids demonstrated good operational applicability and a high compatibility with standard household centrifugal pumps designed for pumping clean single-phase liquids. The waste nanofluids were evaporated under moderate irradiation from the lamps. We stored the remaining deposit of the agglomerated nanoparticles. Our experiments were carried out for 45 days, during which the system was in continuous operation 10...15 hours per day. During this time, the pump did not present any sign of malfunction.

The visual inspection of the rig revealed several places of local contamination of tubes by a thin layer of graphene. Typical places of contamination were associated with local hydraulic resistances: bends, T-junction, extensions, and valves. Most probably, this is due to the influence of several factors: enhanced local body forces (e.g., centrifugal) that increased the deposition of particles, and turbulent diffusion of the particles towards the walls. In addition, the deposits are found where local reduction of shear stress took place in the flow. Therefore, the shear-based removal of the deposited nanoparticles was weaker there than in the rest of the tubes.

The overall contamination of the loop was not intense: the contamination did not reduce the flow area of the circuit pipelines and did not block the pump and control valves. The observed deposit layer was micro-sized. The glass tubes of the DASC and silicone hoses remained transparent even in the presence of contamination. Several examples of deposits found in different regions of the rig are depicted in the Supplementary Materials.

Another very intense deposition of the particles took place in the pump. A thin micro-sized layer of MWCNTs was uniformly distributed over the internal surface of casing of the pump and locally at the impeller. The image of the deposit is presented in the Supplementary Materials. A probable reason for this deposition is the turbulent diffusion of nanoparticles, as the turbulence was most intensive in the pump. We note that the deposition did not influence the operation of the pump. The bottom of the expansion tank was locally covered with a thin layer of particles which were obviously agglomerates deposited under the gravity.

The glass tubes of the DASC were less contaminated. At concentrations of nanofluid below 0.01% wt., contamination was not visually detected. At higher concentrations, contamination was local, and the contaminated areas looked as shown in Fig. 11. The least intensive deposition in the glass tubes might be due to the combination of the following factors: weaker turbulent diffusion and the absence of local flow resistance. Another possible reason might be the difference between Hamaker constants for the glass and the polymer the pump was made of.

Figure 11: Local contamination of glass tubes by nanofluids with MWCNT concentration > 0.01% wt.

After experiments, the main flow loop of the setup was cleaned by pigging and flushing with the water-ethanol mixture (4:1). In the Supplementary Materials, we depict how the system looked after the cleaning procedure. We note that the regular maintenance of the nanofluid-based DASC is not suitable for a solar domestic hot water system. More research should be dedicated towards the development of chemicals suitable for hydraulic flashing of MWCNT deposits.

4.3. Simulations

4.4. Validation

We validate the model by comparing the overall temperature increase in the DASC with the model for different optical alternatives and flow rates. Fig.6 demonstrates that the model-predicted temperature difference reduces with the flow rate due to the shortage of residence time in the collector. To limit the instrumentation uncertainty, we present in Fig. 6 a range between two model outputs where the inlet temperature is subtracted from the average outlet temperature and the spatial position of the outlet temperature sensor. Reading the figure, we conclude that the simulations compare very well with the experiments for the surface absorption case. The average discrepancy is well below 10%, so the CFD-predicted values are always within the interval of experimental uncertainties. The discrepancy increases to an average of 22% when we simulate the volumetric absorption case with water in the DASC. Here the model underpredicts the experiment. The CFD-output at the position of the outlet sensor is just at the tip of the experimental uncertainty interval, which could be due to the non-uniform distribution of radiant heat from the lamps that is not accounted for by the model. A discrepancy may also originate from a mutual reflection of light from the tubes.

The model of the nanofluid-based DASC underpredicts the experiment for the turbulent cases and several CFD-points are outside the interval of experimental uncertainties. The average discrepancy here is not much different for a single-phase case and equals 25%. The sensor-based output is closer to the experiment as for the single-phase case, so the flow patterns of the model correlate with the experiment. The largest deviation is observed in the laminar case, where the difference is 44%. Mixed convection is expected for this flow condition. The regime becomes sensitive to viscosity of the fluid, especially for the MWCNT deposits, which form at the lowest flow rates. Following the simulation results, the deposits may pack up to 0.1% wt. (see Fig.16). The apparent viscosity of the aqueous MWCNT nanofluid may grow by 20% at this concentration [43]. Another source of uncertainty is the cylindrical shape of the particles, which might influence the deposition for the laminar case.

Fig.7 illustrates how the model predicts the temperature difference when altering concentration of particles at a fixed flow rate. It follows from the figure that the model reproduces the experiments well, mostly within the interval of experimental uncertainties. The average discrepancy is 11%. Following the model, the theoretical optimum of the concentration is 0.006% wt. which is a possible value taking into account the resolution of the experimental plot. This concentration corresponds to the experimental observations by Li et al.[27] for a similar collector with MWCNT-based nanofluid. The model overpredicts the experiment at the most dilute concentration. We address this deviation to the discrepancy of fit for the extinction coefficient given in Eq.12.

4.5. Flow patterns

Next, we consider the flow patterns in the DASC focusing on the velocity profiles. They are presented in Fig.12 in terms of the streamlines of flow velocity. The most interesting evolution of the flow takes place in the bend‘s region, which is shown in the figure. Here we observe the centrifugal acceleration of the flow by up to 160% of the average velocity. The acceleration results in the formation of Dean vortices. The vortices twist the velocity profile after the bends, so the minimum of the velocity shifts towards the top surface in the second pipe of the collector. The vortices further interfere, so the maximum goes to the top in the next two pipes. The next round of interference results in a nearly-uniform profile in the rest half of the DASC. The three-dimensional velocity profiles are available in the supplementary Star-View+ (freeware) scene file (Streamlines.sce). We note that the nanoparticles do not influence the velocity profile in the turbulent flow regime due to the low concentration.

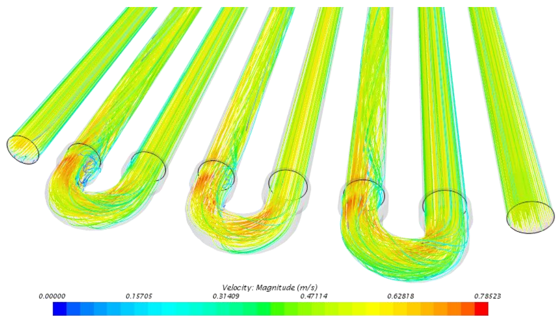

Figure 12: Streamlines of flow velocity at 7.9 l/min

Next, we present the temperature profile where the difference between the opaque surface without nanoparticles and the DASC is clear. There are transversal profiles of the temperature in Fig.13. To account for slightly different temperatures in the tank and the surrounding air, in the figure, we present the results in terms of the reduced temperature $\theta = \left(T - T_i\right) / \left(T_i - T_a\right)$, where indices a and i denote ambient and inlet conditions.

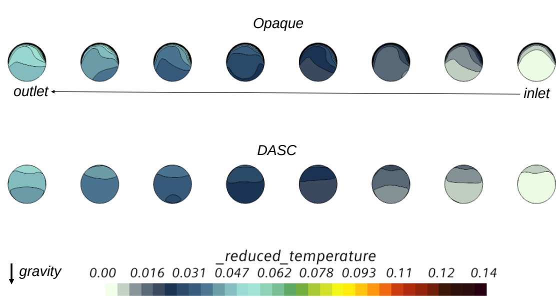

Figure 13: Distribution of reduced temperature in transversal cross-sections in the centre of DASC at ≈ 8 l/min and G = 915 W/m^2. The DASC with 0.01 %wt. is compared to an equivalent case with the opaque top surface with water.

It follows from the figure that the temperature profile is highly non-uniform in the surface absorption case. This is due to the dependence of local heat transfer on flow velocity at the top boundary. As a result, the warmest flow resides in a thin boundary layer adjacent to the top boundary while the bottom layers of fluid are still relatively cold. Therefore, the thermal loss is highest at the top boundary. The temperature profile develops with flow velocity, so the quasi-uniform temperature distribution is detected in the very center of the collector. The temperature gradient restores further downflow.

The temperature profile in the nanofluid-based DASC is different. We detect a sufficiently uniform distribution of temperature in the cross-sections while the maximum is still associated with the top half of the cross-section. The temperature gradient is smaller than in the surface absorption case, and so the thermal leaks are lower for the DASC. The temperature profiles are less dependent on local flow velocity as the fluid's volumetric heating takes place in the DASC. The axial distribution of temperature from Fig.14 demonstrates a continuous temperature increase along the DASC. The detailed three-dimensional temperature profiles are found in the supplementary scene file (T_nanofluid.sce).

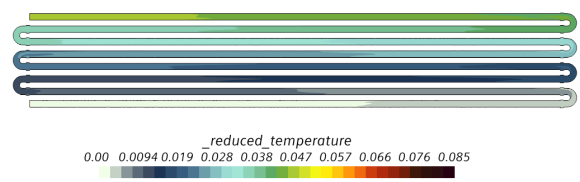

Figure 14: Distribution of reduced temperature in the midline cross-section of the DASC at 7.9 l/min, 0.01 %wt., and G = 915 W/m^2.

4.6. Deposition efficiency

We quantify the total deposition of the nanoparticles in the collector using the deposition efficiency term [40] defined here as the fraction of particles left in the collector. This parameter is presented in Fig.15 for different Reynolds numbers of the flow. Reading the plot, we note the parameter reduces with the flow from 49% in laminar regime down to 1...2% in a turbulent flow. A qualitatively similar trend was observed in [40] for a micro-scale DASC with laminar flow and smaller nanoparticles. However, in the latter case, the maximum efficiency was 7%. Several mechanisms promote the deposition in the model: turbulent diffusion and settling due to gravity and the centrifugal forces in bends. The deposition is mitigated by lift at high flow velocities. The thermophoresis prevents the particles from being deposited at the heated surface while promoting the deposition at the cold bottom wall. The maximum deposition is observed at low Reynolds numbers. In this case, the most important driver of deposition is the body force. In addition, the maximum temperature gradient is established at low flow and so promotes thermophoretic drift towards the cold wall. The lift force is lowest for the low Re.

The present model does not account for Brownian diffusion of the particles. Therefore, it is interesting to order-of-magnitude estimate the influence of this mechanism on the deposition. Here we adopt the expression from Gormley and Kennedy [47, 58] to compute the Brownian deposition efficiency in a pipe of the length equivalent to our DASC:

$$\eta_d = 1 - 0.82e^{-3.66\overline{\mu}} - 0.097e^{-22.2\overline{\mu}} - 0.0135e^{-53\overline{\mu}}, \quad (13)$$

where $\overline{\mu} = 4D_B s / D_p^2 \overline{v}_l$ with the length of the pipes s and mean flow velocity $\overline{v}_l$. The coefficient of Brownian diffusion is taken from Sager [45] as $D_B = k_B \overline{T}_l C_c / 3\pi\mu_l d$ where $\overline{T}_l$ is the collector-average temperature and k_B is the Boltzmann constant. The resulting diffusion coefficient was about $3{\cdot}10^{-12}$ which corresponded to the recent experimental measurements by Rudyak and Tretiakov [59] concerning a similar MWCNT-nanofluid stabilised by sodium dodecylbenzenesulfonate.

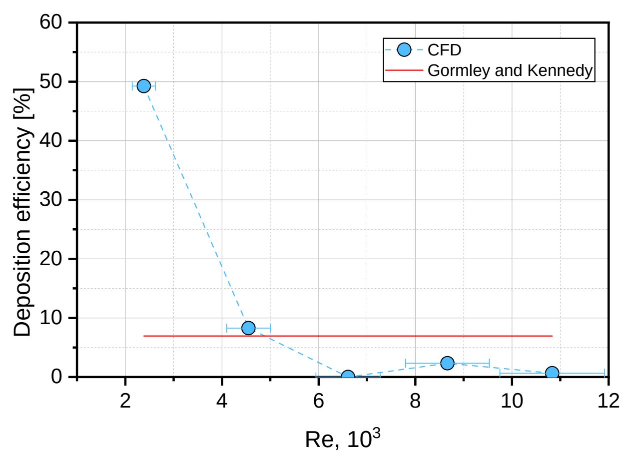

Figure 15: The deposition efficiency as a function of Reynolds number

In Fig.15 we show how the function from Eq.13 depends on Re. It is seen that the sensitivity of the Brownian deposition to the flow in DASC is minimal and is mainly attributed to the change of the mean flow temperature. For high Reynolds numbers, the expression overpredicts the model with a low difference of 3%. This means that the Brownian deposition (Eq.13) and the combination of the turbulent and thermophoretic deposition are of a similar order. However, the model overpredicts Eq.13 by 42% for Re<3000, meaning that the deposition in DASC is not entirely due to the Brownian diffusion to the walls. We attribute the difference to a combined action of centrifugal forces in the bends and the enhanced thermophoresis which are not accounted for in the expression.

We further analyse the model-predicted concentration profiles. They are shown in Fig.16 by iso-surfaces of MWCNT volume fraction (scaled with an inlet value). We depict non-uniform deposition with the 12.5-fold concentration increase in the deposits. The most notable sedimentation happens in the bends and at the bottom surface of the collector. It confirms that the centrifugal force in bends and the gravity are the main drivers of the process. The deposition profiles in the glass tubes are qualitatively similar to those observed experimentally (see e.g., Fig. 11).

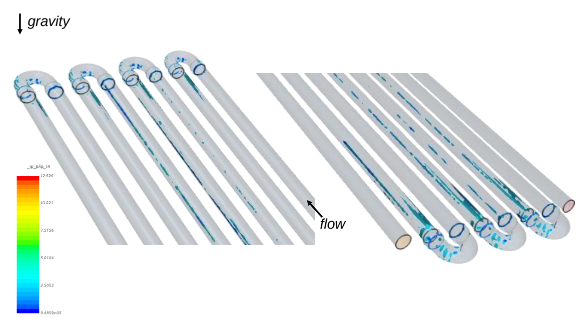

Figure 16: Surface plots of nanoparticle volume fraction in the vicinity of bends at 7.9 l/min, 0.01 %wt., and G = 915 W/m^2. The concentration is scaled with the initial value.

5. Conclusions

The study of the nanofluid-based direct absorption solar collector demonstrated that MWCNTs can significantly increase the efficiency of the solar thermal collection in comparison with the standard technology. The optimum concentration of particles exists, and the optimum was 0.01% wt. in this study. The nanofluid with this concentration allowed for an increase in the efficiency of the solar collector by 5.8...37.9% relative to an equivalent geometry with surface absorption. The increase in thermal efficiency is achieved by reducing heat losses from the collector elements: volumetric light absorption in the nanofluid excludes overheating of the collector surfaces relative to the liquid and equalises the temperature field in bulk. The optimum concentration of particles is closely related to the geometry of the receiver and must be determined individually experimentally or by simulation.

The nanofluid used in the study demonstrated good operational stability. The production of the nanofluid was simple and did not require complex technical solutions. During operation in the collector for 45 days, there was neither a malfunction in the system nor visible mechanical damage or wear of elements. However, there were observed deposits that might lower the long-term performance of the DASC. To address this issue, we tried several routines of mechanical and chemical cleaning of the equipment. The combination of both methods leads to the best result. In addition to good performance characteristics, the nanofluid demonstrated high stability, remaining homogeneous for at least six months after production. The formation of small and easily removable sediment was observed in samples over 0.01 wt%, in which the ratio of surfactant mass to particle mass was the lowest.

The CFD model of the studied DASC with nanofluid was developed. The model was used to provide detailed insight into the flow patterns of the DASC. The model was validated against the experiments with the discrepancy in the range 10...25%. The model demonstrated that, unlike in the previous studies of the flat DASCs, the tubular design of the collector resulted in the intensive mixing of the phases. The flow was well agitated, so the deposition efficiency was less than 5% in the turbulent flow regime.

The model was used to tune-up the composition of the nanofluid theoretically. The model-predicted optimum was slightly lower (0.006%) than in the experiment (0.01%), which was a possible value when accounting for the experimental uncertainties. The simulation of particle deposition resulted with a qualitatively similar sedimentation profile relative to the observed contamination in the experiments. The developed model is a useful tool for designing the nanofluid-based direct absorption collectors.

Acknowledgments

This study was supported by the Russian Science Foundation (project No. 19-79-10083). We thank RPE "Nanotechnology Center" in Moscow for information on MWCNTs and their microscopy. B.V. Balakin thanks Prof. D. Eskin from SkolTech for fruitful discussions on the physics of flows with Brownian motion. P. G. Struchalin thanks I.D. Petrosyan and I.M. Petrosyan for facilitating the logistics of the experiments.

References

[1] Renewables 2020 Global Status Report, REN21, 2020.

[2] International Energy Agency, Share of renewable sources in global heat consumption, 2019, https://www.iea.org/ (2021).

[3] International Energy Agency, Solar heating and cooling programme, https://www.iea-shc.org/ (2021).

[4] S. Gorjian, H. Ebadi, F. Calise, A. Shukla, C. Ingrao, A review on recent advancements in performance enhancement techniques for low-temperature solar collectors, Energy Conversion and Management 222 (2020) 113246. doi:10.1016/j.enconman.2020.113246.

[5] S. K. Verma, N. K. Gupta, D. Rakshit, A comprehensive analysis on advances in application of solar collectors considering design, process and working fluid parameters for solar to thermal conversion, Solar Energy 208 (2020) 1114–1150. doi:10.1016/j.solener.2020.08.042.

[6] N. Abed, I. Afgan, An extensive review of various technologies for enhancing the thermal and optical performances of parabolic trough collectors, International Journal of Energy Research 44 (7) (2020) 5177–5164. doi:10.1002/er.5271.

[7] A. Shafieian, M. Khiadani, A. Nosrati, Strategies to improve the thermal performance of heat pipe solar collectors in solar systems: A review, Energy Conversion and Management 183 (2019) 307–331. doi:10.1016/j.enconman.2018.12.115.

[8] S. Sakhaei, M. Valipour, Performance enhancement analysis of the flat plate collectors: A comprehensive review, Renewable and Sustainable Energy Reviews 102 (2019) 186–204. doi:10.1016/j.rser.2018.11.014.

[9] I. Wole-osho, E. Okonkwo, S. Abbasoglu, D. Kavaz, Nanofluids in solar thermal collectors: Review and limitations, International Journal of Thermophysics 41 (11) (2020). doi:10.1007/s10765-020-02737-1.

[10] P. Visconti, P. Primiceri, P. Costantini, G. Colangelo, G. Cavalera, Measurement and control system for thermosolar plant and performance comparison between traditional and nanofluid solar thermal collectors, International Journal on Smart Sensing and Intelligent Systems 9 (3) (2016) 1220–1242. doi:10.21307/ijssis-2017-915.

[11] G. Colangelo, M. Milanese, A. De Resi, Numerical simulation of thermal efficiency of an innovative Al2O3 nanofluid solar thermal collector influence of nanoparticles concentration, Thermal Science 21 (6) (2017) 2769–2779. doi:10.2298/TSCI151207168C.

[12] P. Raj, S. Subudhi, A review of studies using nanofluids in flat-plate and direct absorption solar collectors, Renewable and Sustainable Energy Reviews 84 (2018) 54–74. doi:10.1016/j.rser.2017.10.012.

[13] M. Potenza, M. Milanese, G. Colangelo, A. de Risi, Experimental investigation of transparent parabolic trough collector based on gas-phase nanofluid, Applied Energy 203 (2017) 560–570. doi:10.1016/j.apenergy.2017.06.075.

[14] E. Sani, L. Mercatelli, S. Barison, C. Pagura, F. Agresti, L. Colla, P. Sansoni, Potential of carbon nanohorn-based suspensions for solar thermal collectors, Solar Energy Materials and Solar Cells 95 (11) (2011) 2994–3000. doi:10.1016/j.solmat.2011.06.011.

[15] V. Khullar, H. Tyagi, N. Hordy, T. P. Otanicar, Y. Hewakuruppu, P. Modi, R. A. Taylor, Harvesting solar thermal energy through nanofluid-based volumetric absorption systems, International Journal of Heat and Mass Transfer 77 (2014) 377–384. doi:10.1016/j.ijheatmasstransfer.2014.05.023.

[16] J. Liu, Z. Ye, L. Zhang, X. Fang, Z. Zhang, A combined numerical and experimental study on graphene/ionic liquid nanofluid based direct absorption solar collector, Solar Energy Materials and Solar Cells 136

(2015) 177–186. doi:10.1016/j.ijheatmasstransfer.2014.05.023.

[17] K. Wang, Y. He, P. Liu, A. Kan, Z. Zheng, L. Wang, H. Xie, W. Yu, Highly-efficient nanofluid-based direct absorption solar collector enhanced by reverse-irradiation for medium temperature applications, Renewable Energy 159 (2020) 652–662. doi:10.1016/j.renene.2020.05.167.

[18] A. Gimeno-Furió, R. Martínez-Cuenca, A. Mondragón, R.and Gasulla, C. Doñate-Buendía, G. Mínguez-Vega, L. Hernández, Optical characterisation and photothermal conversion efficiency of a water-based carbon nanofluid for direct solar absorption applications, Energy 212 (2020) 118763. doi:10.1016/j.energy.2020.118763.

[19] M. Milanese, G. Colangelo, A. Cretì, M. Lomascolo, F. Iacobazzi, A. de Risi, Optical absorption measurements of oxide nanoparticles for application as nanofluid in direct absorption solar power systems – Part I: Water-based nanofluids behavior, Solar Energy Materials and Solar Cells 147 (2016) 315–320. doi:10.1016/j.solmat.2015.12.027.

[20] M. Milanese, G. Colangelo, A. Cretì, M. Lomascolo, F. Iacobazzi, A. de Risi, Optical absorption measurements of oxide nanoparticles for application as nanofluid in direct absorption solar power systems – Part II: ZnO, CeO2, Fe2O3 nanoparticles behavior, Solar Energy Materials and Solar Cells 147 (2016) 321–326. doi:10.1016/j.solmat.2015.12.030.

[21] J. E. Minardi, H. N. Chuang, Performance of a "black" liquid flat-plate solar collector, Solar Energy 17 (3) (1975) 179–183. doi:10.1016/0038-092X(75)90057-2.

[22] Z. Luo, C. Wang, W. Wei, G. Xiao, M. Ni, Performance improvement of a nanofluid solar collector based on direct absorption collection (dac) concepts, International Journal of Heat and Mass Transfer 75 (2014) 262–271. doi:10.1016/j.ijheatmasstransfer.2014.03.072.

[23] H. K. Gupta, G. D. Agrawal, J. Mathur, An experimental investigation of a low temperature Al2O3-H2O nanofluid based direct absorption solar collector, Solar Energy 118 (2015) 390–396. doi:10.1016/j.solener.2015.04.041.

[24] M. Karami, M. Akhavan-Bahabadi, M. Delfani, S.and Raisee, Experimental investigation of CuO nanofluid-based direct absorption solar collector for residential applications, Renewable and Sustainable Energy Reviews 52 (2015) 793–801. doi:10.1016/j.rser.2015.07.131.

[25] S. Delfani, M. Karami, M. Akhavan-Behabadi, Performance characteristics of a residential-type direct absorption solar collector using MWCNT nanofluid, Renewable Energy 87 (1) (2016) 754–764. doi:10.1016/j.renene.2015.11.004.

[26] M. Vakili, S. Hosseinalipour, S. Delfani, S. Khosrojerdi, M. Karami, Experimental investigation of graphene nanoplatelets nanofluid-based volumetric solar collector for domestic hot water systems, Solar Energy 131 (2016) 119–130. doi:10.1016/j.solener.2016.02.034.

[27] Q. Li, C. Zheng, S. Mesgari, Y. L. Hewkuruppu, N. Hjerrild, F. Crisostomo, G. Rosengarten, J. A. Scott, R. A. Taylor, Experimental and numerical investigation of volumetric versus surface solar absorbers for a concentrated solar thermal collector, Solar Energy 136 (2016) 349–364. doi:10.1016/j.solener.2016.07.015.

[28] T. B. Gorji, A. Ranjbar, A numerical and experimental investigation on the performance of a low-flux direct absorption solar collector (dasc) using graphite, magnetite and silver nanofluids, Solar Energy 135 (2016) 493–505. doi:10.1016/j.solener.2016.06.023.

[29] S. Kumar, V. Sharma, M. R. Samantaray, N. Chander, Experimental investigation of a direct absorption solar collector using ultra stable gold plasmonic nanofluid under real outdoor conditions, Renewable Energy 12 (2020) 1958–1969. doi:10.1016/j.renene.2020.10.017.

[30] O. Z. Sharaf, R. A. Taylor, E. Abu-Nada, On the colloidal and chemical stability of solar nanofluids: From nanoscale interactions to recent advances, Physics Reports 867 (2020) 1–84. doi:10.1016/j.physrep.2020.04.005.

[31] N. Sezer, M. A. Atieh, M. Koç, A comprehensive review on synthesis, stability, thermophysical properties, and characterization of nanofluids, Powder Technology 344 (2019) 404–431. doi:10.1016/j.powtec.2018.12.016.

[32] Nanotechnology Center, Multi-walled carbon nanotubes (last visit date 14.01.21), https://dealtom.ru/content/production.

[33] S. Javadian, H. Gharibi, B. Sohrabi, H. Bijanzadeh, M. Safarpour, R. Behjatmanesh-Ardakani, Determination of the physico-chemical parameters and aggregation number of surfactant in micelles in binary alcohol–water mixtures, Journal of Molecular Liquids 137 (1-3) (2008) 74–79. doi:10.1016/j.molliq.2007.04.001.

[34] J. A. Duffie, W. A. Beckman, Solar engineering of thermal processes, John Wiley & Sons, 2013.

[35] National Institute of Standards and Technology, NIST Chemistry WebBook. Water (last visit date 29.01.21), https://webbook.nist.gov/cgi/cbook.cgi?Name=water&Units=SI.

[36] V. N. Stabnikov, I. M. Royter, T. B. Protsuk, Ethanol (in Russian), Food Industry Moscow, 1976.

[37] M. A. Marcos, N. E. Podolsky, D. Cabaleiro, L. Lugo, A. O. Zakharov, V. N. Postnov, N. A. Charykov, S. V. Ageev, K. N. Semenov, MWCNT in PEG-400 nanofluids for thermal applications: A chemical, physical and thermal approach, Journal of Molecular Liquids 294 (2019) 111616. doi:10.1016/j.molliq.2019.111616.

[38] P. G. Kumar, V. Kumaresan, R. Velraj, Experimental investigation on thermophysical properties of solar glycol dispersed with multi-walled carbon nanotubes, Fullerenes, Nanotubes and Carbon Nanostructures 24 (10) (2016) 641–652. doi:10.1080/1536383X.2016.1219852.

[39] M. Wan, R. R. Yadav, G. Mishra, D. Singh, B. Joshi, Temperature dependent heat transfer performance of multi-walled carbon nanotube-based aqueous nanofluids at very low particle loadings, Johnson Matthey Technology Review 59 (3) (2015) 199–206. doi:10.1595/205651315X688163.

[40] R. Bårdsgård, D. M. Kuzmenkov, P. Kosinski, B. V. Balakin, Eulerian CFD model of direct absorption solar collector with nanofluid, Journal of Renewable and Sustainable Energy 12 (2020) 033701. doi:10.1063/1.5144737.

[41] W. M. Rohsenow, J. P. Hartnett, Y. I. Cho, et al., Handbook of heat transfer, Vol. 3, McGraw-Hill New York, 1998.

[42] D. Gidaspow, Multiphase flow and fluidization: continuum and kinetic theory descriptions, Academic press, 1994.

[43] S. Hamze, N. Berrada, A. Desforges, B. Vigolo, J. Gleize, J. Ghanbaja, T. Mare, D. Cabaleiro, P. Estellé, Dynamic viscosity of purified multi-walled carbon nanotubes water and water-propylene glycol-based nanofluids, Heat Transfer Engineering (2020) 1–12.

[44] E. E. Michaelides, Particles, bubbles & drops: Their motion, heat and mass transfer, World Scientific Publishing Co., 2006.

[45] C. Sager, Der Partikeltransport in turbulent durchströmten Rohrleitungen und seine besondere Bedeutung für die Partikelmesstechnik,

2007.
URL https://books.google.no/books?id=l3r4NwAACAAJ

[46] C. T. Crowe, J. D. Schwartzkopf, M. Sommerfeld, Y. Tsuji, Multiphase flows with droplets and particles, CRC press, 2012.

[47] N. Fuchs, The mechanics of aerosols, Pergamon Press, 1964.

[48] T. R. Auton, J. C. R. Hunt, M. Prud'Homme, The force exerted on a body in inviscid unsteady non-uniform rotational flow, Journal of Fluid Mechanics 197 (1988) 241—-257. doi:10.1017/S0022112088003246.

[49] M. Lance, J. Bataille, Turbulence in the liquid phase of a uniform bubbly air–water flow, Journal of Fluid Mechanics 222 (1991) 95—-118. doi:10.1017/S0022112091001015.

[50] A. D. Gosman, C. Lekakou, S. Politis, R. I. Issa, M. K. Looney, Multidimensional modeling of turbulent two-phase flows in stirred vessels, AIChE Journal 38 (12) (1992) 1946–1956. doi:10.1002/aic.690381210.

[51] J. R. Brock, On the theory of thermal forces acting on aerosol particles, Journal of Colloid Science 17 (1962) 768–780. doi:10.1016/0095-8522(62)90051-X.

[52] J. D. Anderson, Computational Fluid Dynamics, The Basics with Applications, McGraw-Hill Education, 1995.

[53] Q. Zhang, G. Chen, S. Yoon, J. Ahn, S. Wang, Q. Zhou, Q. Wang, J. Li, et al., Thermal conductivity of multiwalled carbon nanotubes, Physical Review B 66 (16) (2002) 165440. doi:10.1103/PhysRevB.66.165440.

[54] W. Yi, L. Lu, Z. Dian-Lin, Z. Pan, S. Xie, Linear specific heat of carbon nanotubes, Physical Review B 59 (14) (1999) R9015. doi:10.1103/PhysRevB.59.R9015.

[55] R. A. Taylor, P. E. Phelan, T. P. Otanicar, R. Adrian, R. Prasher, Nanofluid optical property characterization: towards efficient direct absorption solar collectors, Nanoscale research letters 6 (1) (2011) 1–11. doi:10.1186/1556-276X-6-225.

[56] NPOMASH, Flat-plate solar collector SOKOL-EFFECT (last visit date 14.12.20), http://www.sokolnpo.ru/.

[57] Viessmann Manufacturing Company, Vacuum tube solar collector "Vitosol 200-T SP2A" (last visit date 14.12.20), https://www.viessmann-us.com/en/residential/solar/tube-collectors/vitosol_200-t_sp2a.html.

[58] P. Gormley, M. Kennedy, Diffusion from a Stream Flowing Through a Cylindrical Tube, Proceedings of the Royal Irish Academy. Section A, Hodges, Figgis & Company, 1949.

[59] V. Rudyak, D. Tretiakov, On diffusion of single-walled carbon nanotubes, Thermophysics and Aeromechanics 27 (2021) 847–855. doi:10.1134/S0869864320060062.